PAPER

Check for updates

Induced magnetic field in sp-hybridized carbon rings: analysis of double aromaticity and antiaromaticity in cyclo[2*N*]carbon allotropes†

Nickolas D. Charistos [ID] *[a] and Alvaro Muñoz-Castro [ID] *[b]

The induced magnetic field of C_{2N} (N = 3–14) carbon rings was dissected to contributions from out-of-plane and in-plane π orbitals revealing two concurrent long range shielding or deshielding cones as a manifestation of the dual aromatic and antiaromatic character of C_{4n+2} and of C_{4n} rings respectively. Aromaticity based on the magnetic criterion was evaluated with regard to the bonding pattern and geometrical characteristics that elucidate the influence of bond length and bond angle alteration on out-of-plane and in-plane magnetic responses. Ground state polyynic geometries of C_{4n+2} rings exhibit comparable shielding cones to annulenes, decreasing the magnetic response with regard to the ring size and similar π_{out} and π_{in} diatropicity. Transition state cumulenic rings display increased aromaticity expressed by a very strong constant magnetic response and augmented π_{out} diatropicity with regard to π_{in}. The variations of the induced magnetic field are explained on the basis of frontier orbital interactions through rotational excitations, which enable further rationalization of the aromatic/antiaromatic behavior.

Introduction

Since the discovery of buckminsterfullerene C_{60} in 1985,[1] research on sp^2 carbon allotropes such as fullerenes, graphenes[2] and carbon nanotubes[3] has sparked the interest on the design and synthesis of a plethora of novel carbon-based nanomaterials with exceptional diversity and applications in numerous fields such as optoelectronics, gas separation, energy conversion and shortage, catalysis and medicine.[4–12] Around the same time research on different carbon allotropes with mixed sp^2–sp hybridization[13] or solely sp hybridized carbon atoms[14] has paved the way for the discovery of new all carbon species with promising applications such as graphdiynes[15–17] and carbon rings.[18]

Early in 1989 Diederich *et al.* reported the gas phase generation of a highly reactive C_{18} cyclocarbon[14] in which each carbon atom was bonded to two other carbons, in contrast to sp^2 hybridized allotropes where the bonding pattern involves three-coordinated carbon atoms. The main question that evolved to a controversy by conflicting theoretical studies was on the

bonding pattern of C_{18}: is it polyynic with altering triple and single bonds, or cumulenic with equal bond lengths? Pure and hybrid DFT[19–21] as well as MP2[22,23] calculations predict cumulenic structures, whereas HF,[14,24] quantum Monte Carlo[25] and CCSD[26] calculations predict polyynic geometries. Further studies diagnosed that the DFT calculated bonding pattern depends on the amount of HF exchange of the hybrid functional,[27,28] whereas range-separated exchange nonempirical DFT schemes provide polyynic structures regardless of the type of functional that is used.[29] Finally in 2019 Kaiser *et al.*[18] isolated by on-surface synthesis and structurally characterized C_{18} using atomic force microscopy (AFM), revealing a polyynic structure with altering single–triple CC bonds putting an end to the controversy.[23,24] Moreover, the cumulenic structure has been predicted to be a transition state between two degenerate polyynic ground states with inverted single–triple bonds.[25,28,30]

A unique characteristic of sp-hybridized carbon structures is the presence of two perpendicular π-electron systems[31] extending the capabilities from sp^2-hybridized carbon structures which sustain a single π-system. Diederich proposed that C_{18} benefited from two distinctive sets of delocalized π electrons,[14] one from out-of-plane (π_{out}) and the other from in-plane (π_{in}) oriented 18π orbitals (Fig. 1), both obeying Huckel's $4n + 2$ rule, which is expected to exhibit interesting electron acceptor properties.[27] The presence of double aromaticity for C_{4n+2} and antiaromaticity for C_{4n} cyclocarbons was confirmed *via* ring current analysis by Fowler *et al.*,[19] while the large NICS values reported by Suresh[20] also imply the existence of double aromaticity given by the two

[a] *Aristotle University of Thessaloniki, Department of Chemistry, Laboratory of Quantum and Computational Chemistry, Thessaloniki, 54 124, Greece. E-mail: nicharis@chem.auth.gr*

[b] *Laboratorio de Química Inorgánica y Materiales Moleculares, Facultad de Ingeniería, Universidad Autonoma de Chile, Llano Subercaceaux 2801, San Miguel, Santiago, Chile. E-mail: alvaro.munoz@uautonoma.cl*
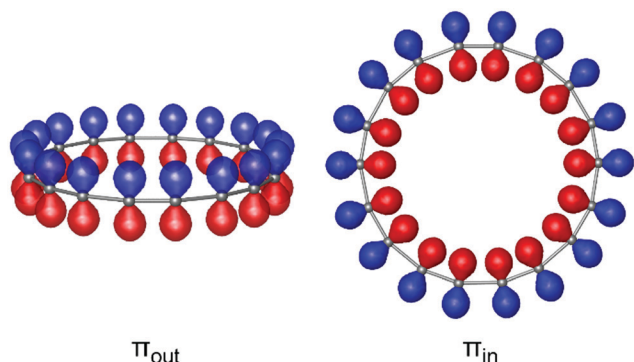
Fig. 1 Illustration of two orthogonal sets of p orbitals of C_{18} ring displaying perpendicular to the plane (π_{out}) and in-plane (π_{in}) orientations.

perpendicular π-systems. The double aromaticity of small carbon rings and related boron–carbon molecules was also confirmed with the CMO-NICS analysis put forth by Schleyer et al.[32] However, studies on the aromaticity of carbon rings were performed on cumulenic structures and the effect of bonding pattern on the magnetic response was not evaluated. Recently Baryshnikov et al.[28] employed the GIMIC method to measure the ring currents of both polyynic and cumulenic configurations of C_{18} and reported that the polyynic structure induces a strong diatropic current which is however much weaker than the diatropic current of cumulene. Moreover, although the GIMIC method does not yet allow the dissection of ring current to contributions from different sets of orbitals, it obtained the current strengths of π_{out} and π_{in} sets by integrating the current density within distinctive contours and found that π_{out} orbitals induce stronger diatropic currents than π_{in}, both in polyynic and cumulenic geometries.

Herein, we study the distinctive characteristics of double aromaticity and antiaromaticity based on the magnetic criterion[33] from cyclo[2N]carbon allotropes, given by their peculiar perpendicular π-systems. However we note that a thorough investigation of the aromaticity requires to take into consideration both electronic and energetic criteria.[34–36] We perform a detailed analysis of the magnetic response of C_{2N} (N = 3–14) rings which is directly related to the aromatic/antiaromatic behavior,[37–42] by means of canonical orbital contributions to the induced magnetic field (CMO-IMF) that allows the through-space visualization of shielding and deshielding cones induced by different sets of orbitals, as well as from each CMO.[43–46] Hence the magnetic field induced from each π_{out} and π_{in} set was visualized for polyynic and cumulenic geometries of C_{4n+2} rings, as well as for those of C_{4n} rings, revealing the trends of the magnetic response of each set of MOs and the effect of ring size, bond length and bond angle. Our results show that polyynic geometries induce a cumulative magnetic field from both sets which is comparable to annulenes and declines with the evolution of ring size, whereas cumulenes induce a much stronger magnetic field independent of the ring size. Accordingly, C_{4n} rings display decreasing deshielding cones for both sets with regard to the ring size. These trends are associated with the inherent bonding pattern and geometrical characteristics of carbon rings, which are further

explained on the basis of frontier orbital interactions through rotational excitations.

Computational methods

A number of various exchange–correlation functionals (XCs) were tested for the optimization of C_{18} (see ESI,† Table S1). Functionals with a high percentage of HF exchange (HFX > 50%) yielded polyynic structures, whereas pure GGAs and functionals with a low percentage of HFX resulted in cumulenic structures with no bond length alteration (BLA) (Table S1, ESI†). In this work we have chosen the use of the range-separated hybrid ωB97XD[47] for the optimization of the C_{2N} (N = 3–14) molecules because it correctly reproduces the experimentally realized[18] polyynic geometry of C_{18} and it has been reported to have the best performance among other functionals for the description of polyynic structures.[48] Moreover, long-range corrected XC functionals like ωB97XD have been found to provide a better description of the cyclic electron delocalization in monocyclic and polycyclic aromatics with regard to conventional XC functionals.[36] All geometry optimizations were carried out with Gaussian09[49] using the 6-311++G(d,p) Gaussian basis set.

Nucleus independent chemical shieldings (NICS) were calculated within the GIAO formalism using several functionals, as detailed in ESI,† and the triple-ζ slater type basis set with two polarization functions (TZ2P) employing the ADF2019 software.[50,51] BHandHLYP[52] was chosen for the quantitative analysis of dissected $NICS_{zz}$ because it performs in very good agreement with ωB97XD (Table S2 and Fig. S2, ESI†) and it is available for the CMO analysis of the chemical shift in ADF. The computationally affordable PBE[53] was chosen for the qualitative analysis of the induced magnetic field. Although the PBE was found to overestimate the NICS, especially in polyynic structures, it accurately reproduces the qualitative features of the magnetic response with regard to the ring size and bonding pattern of C_{2N} rings (see ESI,† Fig. S2 and S3). Chemical shieldings were dissected to contributions from canonical MOs (CMOs) employing the NMR and EPR modules[54] of the ADF and the contributions of π_{out} and π_{in} sets of orbitals were constructed by the summation of the corresponding CMOs.

For the calculation of the induced magnetic field the molecules were placed on xy Cartesian plane and the chemical shielding was calculated in a 31^3 cubic grid of points with a separation step of 0.5 Å. Extraction of CMO contributions at each point and generation of cube files per MO were performed with our custom MIMAF code.[55] Visualization of induced magnetic field isosurfaces was performed with the VMD.[56]

Results and discussion

Geometrical characteristics

The ground state optimized geometries of C_{4n+2} (n = 1–6) and C_{4n} (n = 2–6) molecules are shown in Fig. S1 (ESI†) and their corresponding geometrical parameters are given in Table 1.

This journal is © the Owner Societies 2020

Phys. Chem. Chem. Phys., 2020, 22, 9240–9249 | 9241
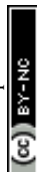
Table 1 Geometrical parameters of C_{2N} ($N = 3$–14) rings optimized at the ωB97XD/6-311++G(d,p) level

| Molecule	Point Group	d_1 (Å)	d_2 (Å)	BLA[a]	θ_1 (°)	θ_2 (°)	BAA[b]
C_6	D_{3h}	1.321		0.00	149.2	90.8	58.4
C_8	C_{4h}	1.384	1.251	0.133	162.8	107.2	55.6
C_{10}	D_{5h}	1.290	1.290	0.00	165.0	123.0	42.1
C_{12}	C_{6h}	1.359	1.234	0.126	168.3	131.7	36.6
C_{14}	C_{7h}	1.307	1.256	0.051	167.0	141.6	25.4
C_{14} TS	D_{7h}	1.281		0.00	168.1	140.5	27.6
C_{16}	C_{8h}	1.364	1.216	0.148	158.9	156.1	2.8
C_{18}	C_{9h}	1.346	1.223	0.123	160.2	159.8	0.4
C_{18} TS	D_{9h}	1.277		0.00	169.4	150.6	18.8
C_{20}	C_{10h}	1.358	1.216	0.141	162.6	161.4	1.2
C_{22}	C_{11h}	1.351	1.219	0.132	164.5	162.8	1.7
C_{22} TS	D_{11h}	1.276		0.00	171.0	156.3	14.8
C_{24}	C_{12h}	1.355	1.216	0.139	165.8	164.2	1.7
C_{26}	C_{13h}	1.352	1.217	0.135	167.0	165.3	1.7
C_{26} TS	D_{13h}	1.276		0.00	172.7	159.6	13.1
C_{28}	C_{14h}	1.354	1.216	0.138	168.0	166.3	1.7

[a] Bond length alteration, $d_1 - d_2$. [b] Bond angle alteration, $\theta_1 - \theta_2$.

All molecules adopt $C_{(n/2)h}$ point group symmetry representing polyynic structures with altering bond lengths and altering bond angles, except for C_6 and C_{10} which adopt $D_{(n/2)h}$ cumulenic structures with equal bond lengths and altering angles. The bond length alteration (BLA) ranges from 0.123 Å to 0.148 Å for all $C_{(n/2)h}$ point group molecules, except for C_{14} which presents a minimal BLA of 0.051 Å. On the other hand, bond angle alteration (BAA) is very large for small rings starting from 58.4° and 55.6° for C_6 and C_8, respectively, and decreases rapidly as the ring size increases, reaching a constant value of 1.7° for C_{2N} ($N = 11$–14), while the smallest BAA (0.4°) is observed in C_{18}. For C_{4n} molecules $D_{(n/2)h}$ geometries with altering bond lengths and equal bond angles were found to be first-order saddle points, whereas higher symmetry D_{nh} geometries with equal bonds and angles were found to be higher-order saddle points for both C_{4n+2} and C_{4n} molecules.

For C_{4n+2} ($n = 3$–6) molecules, QST2 and IRC calculations generated cumulenic geometries with equal bond lengths and altering bond angles, adopting $D_{(n/2)h}$ point group symmetry, as transition states between two inversion related polyynic ground states[28] (Fig. 2). The transition states display increased BAA with regard to the respective ground states. The energy barrier for the inversion increases with the number of carbon atoms, starting from a marginal barrier of 0.12 kcal mol^{-1} for C_{14} and reaching 10.90, 24.42 and 37.54 kcal mol^{-1} for C_{18}, C_{22} and C_{26} respectively.

Total magnetic response

When an (anti)aromatic molecule is subjected to a uniform external magnetic field $\vec{B}^{ext}$, then closed circuits of mobile electrons induce a current density, which in turn induces a secondary magnetic field, $\vec{B}^{ind}$, either opposing (shielding) the external field in aromatic rings or reinforcing (deshielding) the external field in antiaromatic rings. In planar structures the molecule is oriented such that the molecular plane (xy) is perpendicular to the external field's direction (z), and hence the induced magnetic field is designated as $\vec{B}_z^{ind}$. The induced
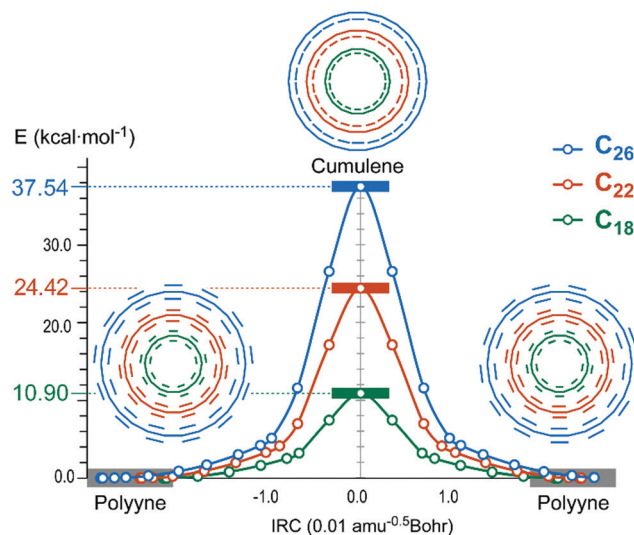
Fig. 2 Relative IRC profiles of C_{18}, C_{22} and C_{26} depicting the interchange of single–triple bonds of polyynic ground states through a cumulenic transition state.

magnetic field is typically visualized as isosurfaces of B_z^{ind}, forming long range shielding or deshielding cones in aromatic or antiaromatic rings respectively. The value of B_z^{ind} isosurface at any point is equal to the zz tensor component of nucleus independent chemical shift, NICS$_{zz}$.

NICS$_{zz}$ values, presented in Table 2 and Fig. S2 (ESI†), reveal the characteristic features of carbon rings' magnetic response. These features are as follows: (a) C_{4n+2} molecules display large diatropic (negative) NICS$_{zz}$ representative of aromatic character, whereas C_{4n} molecules display large paratropic (positive) NICS$_{zz}$ representative of antiaromatic character; (b) NICS$_{zz}$ of polyynic C_{4n+2} ($n = 3$–6) and C_{4n} molecules decreases significantly as the ring size increases; (c) NICS$_{zz}$ of the cumulenic C_{4n+2} ($n = 1$–6) geometries increases with the ring size, showing a trend to reach a maximum value at larger rings; (d) accordingly for C_{4n+2} molecules there is an increasing difference in NICS$_{zz}$ between polyynic ground states and cumulenic transition states with an increment in the ring size; (e) the maximum NICS$_{zz}$ among

Table 2 Total NICS$_{zz}$ values (ppm) and contributions from π_{out} and π_{in} orbitals of C_{2N} carbon rings and reference molecules computed at the BHandHLYP/TZ2P level

Molecule	Total	π_{out}	π_{in}	Molecule	Total	π_{out}	π_{in}
C_6	−37.7	−39.8	19.2	C_8	130.9	110.5	28.2
C_{10}	−65.2	−52.1	−3.3	C_{12}	96.8	64.8	34.1
C_{14}	−81.6	−49.9	−25.4	C_{16}	57.9	27.0	31.7
C_{14} TS	−89.2	−56.7	−25.0	C_{20}	33.4	15.5	18.7
C_{18}	−44.7	−20.6	−16.4	C_{24}	18.7	8.6	10.8
C_{18} TS	−101.5	−58.3	−37.2	C_{28}	10.5	4.8	6.4
C_{22}	−22.0	−10.7	−7.8				
C_{22} TS	−104.0	−58.1	−40.7				
C_{26}	−10.9	−5.4	−3.4				
C_{26} TS	−99.3	−55.8	−39.0				
C_6H_6	−15.9	−36.7					
$C_{18}H_{18}$	−41.5	−48.0					
$C_{18}H_6$	−8.1	−12.7	−15.7				
B_9H_9	3.3	0.5	3.4				

9242 | *Phys. Chem. Chem. Phys.*, 2020, **22**, 9240–9249

This journal is © the Owner Societies 2020

ground state C_{4n+2} molecules is observed in C_{14} which presents the minimum BLA.

The above remarks clarify controverting NICS studies of C_{4n+2} rings.[19,20] The NICS values reported by Fowler *et al.* show an increment in diatropic NICS of C_{4n+2} for $n = 1–5$ and then a significant decrement for $n = 6, 7$ due to molecular geometry obtained with B3LYP functional which predicts cumulenic structures for $n = 1–5$ and polyyinic structures for $n = 6, 7$.[19] On the other hand, Suresh and Remya reported increasing diatropic NICS values for all C_{4n+2} ($n = 1–7$) trending to a maximum value due to cumulenic geometries obtained with MO6L functional.[20]

Visualizations of B_z^{ind} induced by all electrons of C_{2N} molecules are presented in Fig. 3 using multiple clipped isosurfaces (± 5 ppm and ± 20 ppm) to depict the long-range effect, as well as a full isosurface of large B_z^{ind} values to illustrate specific characteristics of the magnetic response close to the molecular domain. C_{4n+2} molecules induce strong long-range shielding cones representative of strong aromatic character. The long-range shielding cone (cyan, -5 ppm) of C_{4n+2} molecules increases with the ring size but the actual trend is revealed by inspection of the strong response close to the molecular plane depicted with green isosurfaces (-50 ppm) in Fig. 3. In ground state polyyinic structures the extension of the short-range response increases from C_{10} to C_{14} where it reaches a maximum

span forming a uniform shielding cone, and then gradually decreases from C_{18} to C_{26}, deforming to a toroidal shape inside the ring of C_{26}. On the contrary the strong shielding cone of cumulenic transition states retains its uniform long range shape. Therefore, the weakening of the magnetic response in ground states is attributable to polyyinic bonding and is irrelevant to the ring size. However, the discrepancy in the magnetic response between ground and transition states for C_{18}, C_{22} and C_{26} is apparently evolving with the ring size. Thus, according to the magnetic criterion, the aromaticity of polyyinic C_{4n+2} decreases for $n > 3$ while it is retained for the respective cumulenic transition states.

C_{4n} molecules sustain strong long-range deshielding cones representative of strong antiaromatic character. However strong short-range response (+60 ppm) decreases with the evolution of ring size, starting with extended uniform deshielding cones in C_8 and C_{12} and downgrading to a toroidal shape in C_{24}, which implies the weakening of antiaromaticity.

Magnetic responses of π_{out} and π_{in} orbitals

The total magnetic response suggests the (anti)aromatic character of C_{2N} carbon rings but does not give any clear information about the source of the long range (de)shielding cones and the individual role of each (para)diatropic circuit in the double aromatic character, because it is constructed by contributions from all π_{out},
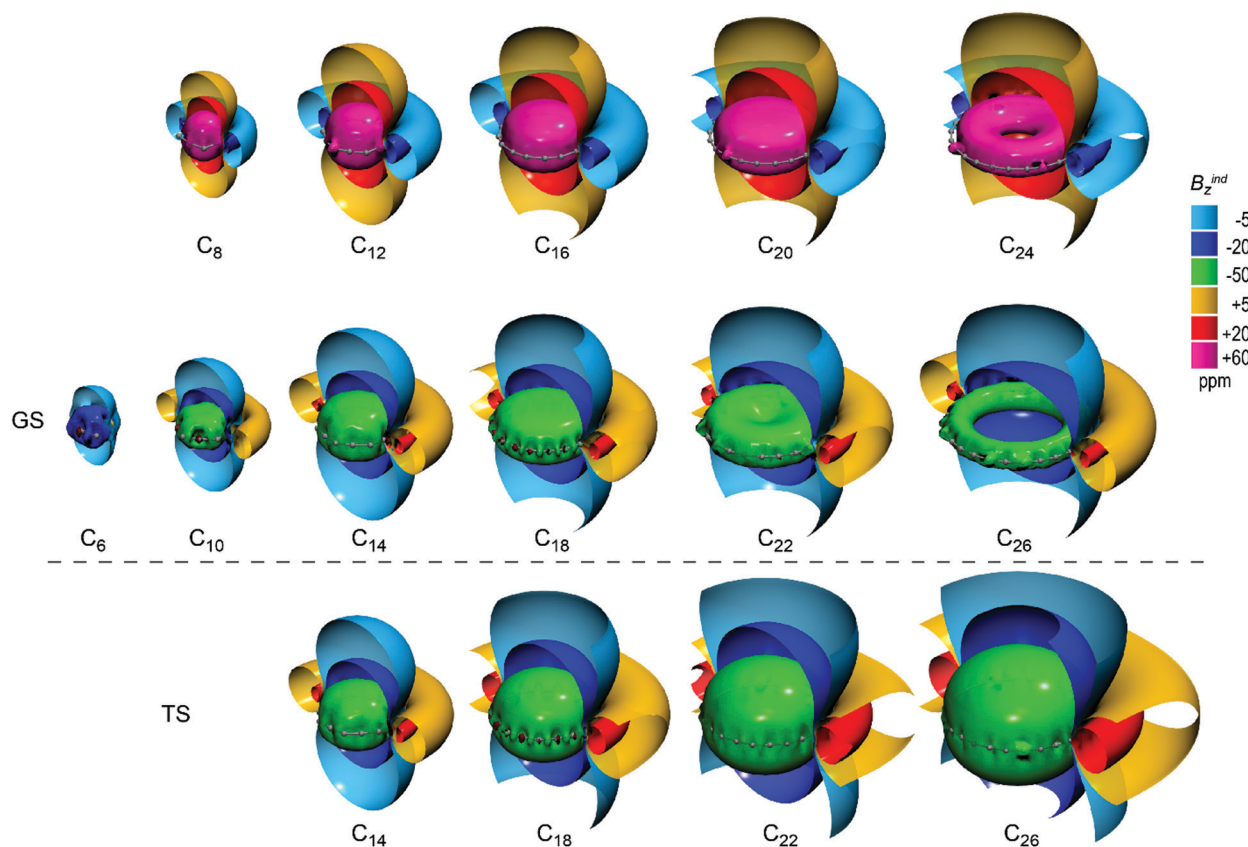

Fig. 3 Isosurfaces of total B_z^{ind} of transition states $D_{(n/2)h}$ C_{4n+2} ($n = 3–6$) (bottom row), ground states $C_{(n/2)h}$ C_{4n+2} ($n = 1–6$) (middle row) and C_{4n} ($n = 2–6$) (top row).

This journal is © the Owner Societies 2020

Phys. Chem. Chem. Phys., 2020, **22**, 9240–9249 | **9243**

π_{in}, σ and core orbitals. In order to gain insight into the origins and the duality of the (anti)aromatic character of C_{2N} carbon rings, we dissected the magnetic response to contributions from π_{out} and π_{in} sets of orbitals, which are exclusive sources of the strong long-range magnetic response.

In Fig. 4, the respective magnetic responses of π_{out} and π_{in} sets of orbitals of ground states C_{4n+2} molecules are given. It is clear that for C_{14} and larger rings, both π_{out} and π_{in} orbitals induce long range shielding cones, illustrating the dual source of their diatropicity. Smaller members C_6 and C_{10} display no or a very weak in-plane magnetic response, respectively, due to a large bond angle alteration (BAA) which leads to a small in-plane orbital overlap. Specifically, the π_{out} orbitals of C_6 induce a shielding cone very similar to benzene and have comparable π_{out}–NICS$_{zz}$ values (−39.8 and −36.7 ppm for C_6 and C_6H_6 respectively). The π_{in} orbitals of C_6 induce a weak short range diatropic response with a paratropic sphere inside the ring (+19.2 ppm at ring center), which is representative of localized CC σ bonding.[43] Therefore, C_6 displays equal diatropicity with benzene originating from the out-of-plane π system, and the large difference in their total NICS$_{zz}$ does not arise from delocalized electrons but from localized σ bonds which have larger paratropic contributions in benzene. C_{10} presents a strong long-range shielding cone induced from π_{out} orbitals with −52.1 ppm contributions at the ring center, and a considerably weaker shielding cone induced from π_{in} orbitals with only −3.3 ppm at the ring center, denoting a marginal in-plane π magnetic response due to a large BAA.

C_{14} induces long range shielding cones from both π_{out} and π_{in} orbitals but the out-of-plane response is much stronger than that of the in-plane, as π_{out} forms an extended uniform −40 ppm isosurface, while π_{in} forms a condensed shielding toroid inside the ring and the π_{out}–NICS$_{zz}$ (−49.9 ppm) is the double of π_{in}–NICS$_{zz}$ (−25.4 ppm). This difference is attributed to the geometry of C_{14}, which presents the minimum BLA that favors the out-of-plane delocalization and significant BAA that hinders the in-plane delocalization. The corresponding transition state displays an almost identical magnetic response, both

in terms of shielding cones and NICS$_{zz}$ values, due to small structural differences in the two states.

For the ground states of larger rings C_{18}, C_{22} and C_{26}, π_{out} and π_{in} display very similar shielding cones. The π_{in}–NICS$_{zz}$ is only 2–4 ppm less diatropic than π_{out}–NICS$_{zz}$, denoting a marginally increased out-of-plane magnetic response. The diatropicity decreases with an increment in the ring size for both sets of orbitals. Specifically NICS$_{zz}$ of π_{out} (π_{in}) decrease from −20.6 (−16.4) ppm in C_{18} down to −10.7 (−7.8) and −5.4 (−3.4) ppm in C_{22} and C_{26} respectively.

In order to assess the C_{18} diatropicity we used as reference three prototypical molecules with 18-π electrons and varying degrees of aromaticity, namely 18-annulene, 18-dehydroannulene and the BN analogue[57] B_9N_9, as presented in Fig. 5. Compared to the π response of 18-annulene (Fig. 5b), the π_{out} of C_{18} induces a weaker shielding cone and presents less than half NICS$_{zz}$, denoting a considerable weaker out-of-plane magnetic response in C_{18}. If we consider both π_{out} and π_{in} orbitals of C_{18}, their cumulative shielding cone (Fig. 5a) is greater than $B_{\pi z}^{ind}$ of 18-annulene, but this is due to the overestimation of PBE which predicts a total ($\pi_{out} + \pi_{in}$)–NICS$_{zz}$ value 21 ppm to be more diatropic than NICS$_{\pi zz}$ of $C_{18}H_{18}$, while with BHandHLYP it is 11.0 ppm less diatropic. Therefore, C_{18} displays a similar or a slightly weaker diatropicity when compared to $C_{18}H_{18}$. Furthermore, 18-dehydroannule (Fig. 5c) is less aromatic than C_{18} and induces a weaker π_{out} shielding cone (π_{out}–NICS$_{zz}$ is −12.7 ppm), as well as a weak short-range paratropic response from 12 π_{in} electrons (π_{in}–NICS$_{zz}$ is +15.7 ppm). Finally, B_9N_9 (Fig. 5d) is a characteristic example with extreme localized electrons, with both 18 π_{out} and 18 π_{in} electrons inducing weak short range diatropic cones strictly positioned on nitrogen atoms. Hence C_{4n+2} ($n > 3$) carbon rings, although they exhibit dual source of diatropicity, show that their magnetic responses are comparable to those of classical π-aromatic annulenes.

The magnetic responses of transition states, presented in Fig. 6, display constant strong shielding cones of both π_{out} and π_{in}. Specifically, π_{out}–NICS$_{zz}$ retains a value of around −57 ppm, whereas π_{in}–NICS$_{zz}$ amounts to $\sim$ −39 ppm for all transition

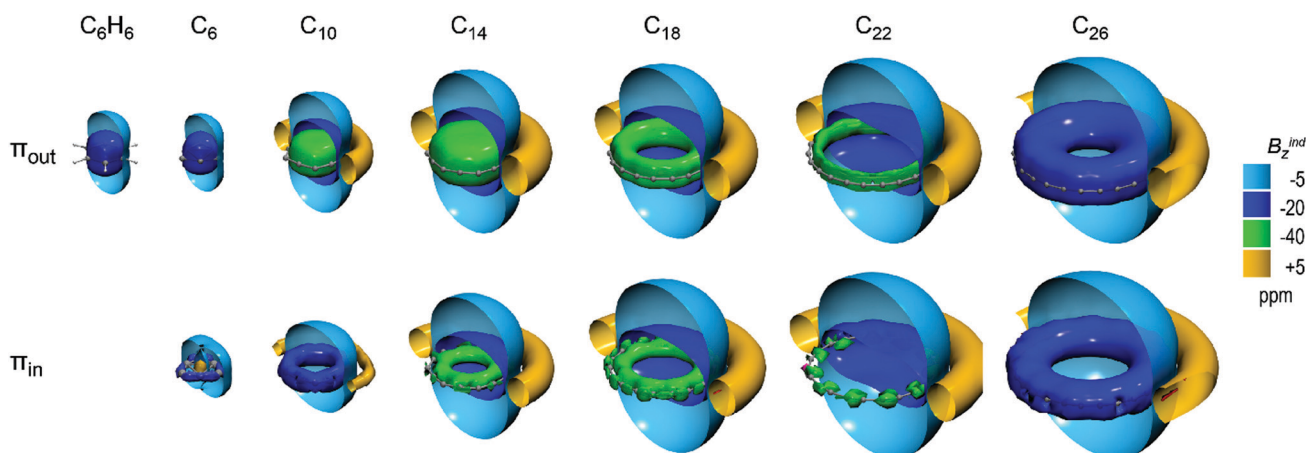**Fig. 4** Isosurfaces of π_{out} (top) and π_{in} (bottom) contributions to B_z^{ind} of polyynic ground states of $C_{(n/2)h}$ C_{4n+2} (n = 1–6) rings.

9244 | *Phys. Chem. Chem. Phys.*, 2020, **22**, 9240–9249
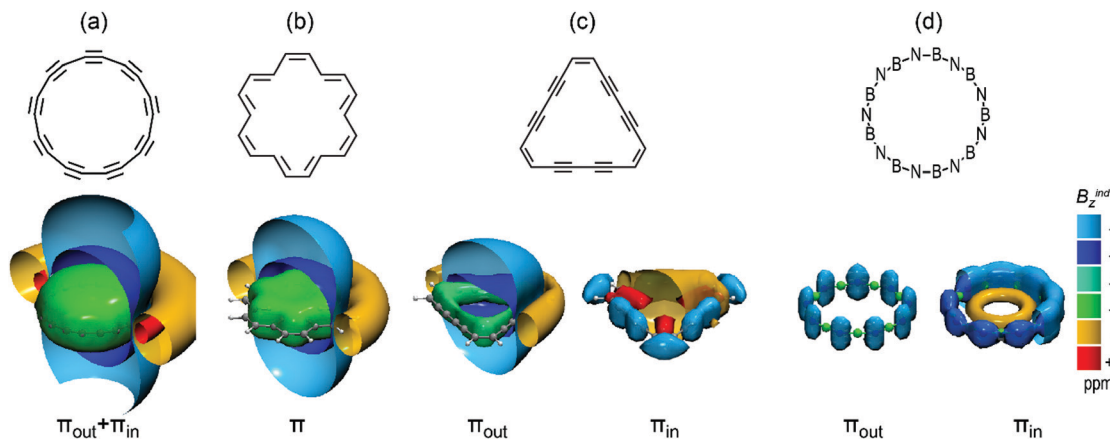
This journal is © the Owner Societies 2020

Fig. 5 Isosurfaces of π contributions to B_z^{ind} of (a) C_{9h} C_{18}, (b) 18-annulene, (c) 18-dehydroannulene and (d) B_9N_9.

states, implying favorable π_{out} delocalization. The difference in π_{out} and π_{in} can be explained by the increased BAA of cumulenic structures which hinders the in-plane overlap. Indeed, the third-order saddle point D_{18h} geometry of C_{18} with zero BLA and BAA presents almost equal π_{out} and π_{in} $NICS_{zz}$ values (-60.2 and -58.7 ppm respectively). However, π_{in} electrons in cumulenic geometries are still more diatropic than polyynic. Hence BLA is the main factor that constrains both π_{out} and π_{in} magnetic responses and BAA affects secondarily only the π_{in} magnetic response. Consequently, the cumulenic geometries are very diatropic from both sources of magnetic response.

Concerning the antiaromatic C_{4n} ($n = 2$–6) rings, both π_{out} and π_{in} orbitals induce equivalent long range deshielding cones (Fig. 7), except for C_8 which exhibits only π_{out} deshielding cone and a weak short range paratropic response of π_{in} due to large BAA, which does not justify a paratropic in-plane ring current. The π_{in} response of C_{14} is also weak due to large BAA but still forms a deshielding cone denoting weak in-plane paratropic current, whereas for larger rings π_{out} and π_{in} induce equivalent deshielding cones. The π_{out} deshielding cones of C_8 and C_{12} are comparable to that of planar C_8H_8 but decline significantly for

larger rings, as the π_{in} deshielding cones also do. Hence, C_{4n} ($n = 3$–6) rings exhibit a dual source of paratropicity representative of antiaromatic character which weakens significantly with an increment in the ring size.

CMO contributions

In order to elucidate the above remarks, we have to take into consideration the electronic structure of carbon rings, especially the frontier orbitals that principally determine the overall magnetic response. Dissection of the induced magnetic field to CMO contributions reveals that lower energy valence orbitals induce a diatropic response, whereas the highest occupied orbitals dictate the overall magnetic response.[43,44] Indeed in C_{2N}, the contributions of π_{out} and π_{in} to $NICS_{zz}$ are linearly correlated to the contribution of the corresponding HOMOs ($R^2 = 0.97$, Fig. S4, ESI†). Hence the (para)diatropicity can be analyzed in terms of HOMO contributions, as given in Table S4 and Fig. S5, S6 (ESI†).

Generally, in antiaromatic molecules the HOMOs induce a very strong paratropic response that overwhelms the diatropicity

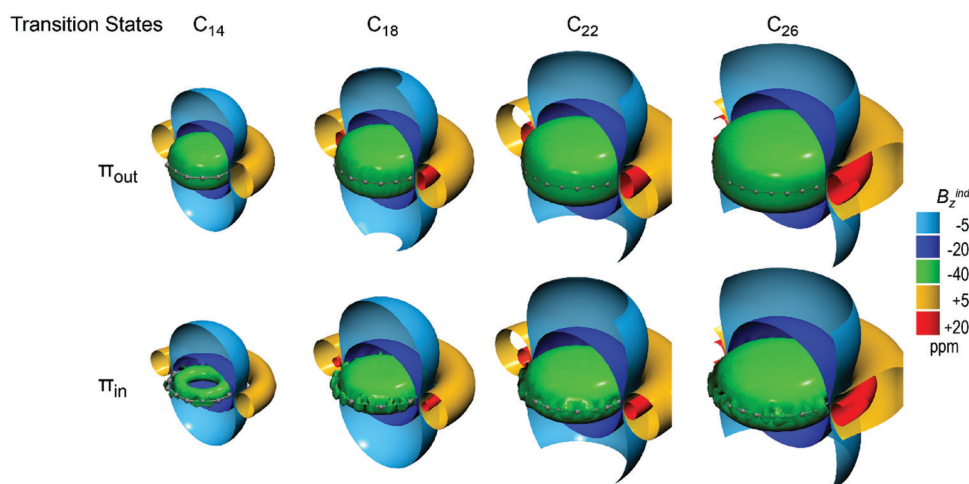
Fig. 6 Isosurfaces of π_{out} (top) and π_{in} (bottom) contributions to B_z^{ind} of cumulenic transition states of $D_{(n/2)h}$ C_{4n+2} ($n = 3$–6) rings.

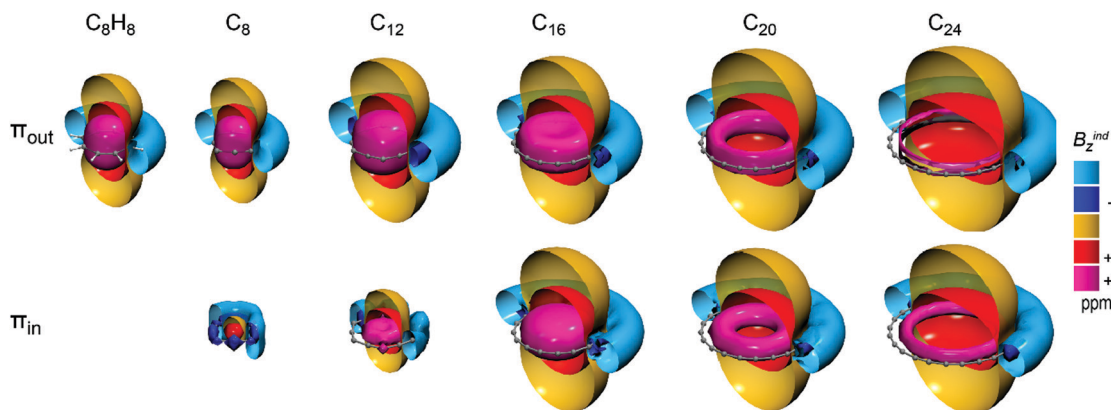This journal is © the Owner Societies 2020

Phys. Chem. Chem. Phys., 2020, **22**, 9240–9249 | **9245**

Fig. 7 Isosurfaces of π_{out} (top) and π_{in} (bottom) contributions to B_z^{ind} of C_{4n} ($n = 2-6$) rings and planar C_8H_8.

of lower orbitals, whereas in aromatic molecules the HOMOs induce a very weak paratropic or diatropic response that adjusts the overall diatropicity and tunes the aromaticity. In turn, the paratropic response of HOMOs originates from symmetry allowed rotational excitations to unoccupied orbitals and its magnitude depends on the energy gap and the overlap of interacting orbitals.[43,44,46,58–60]

In C_{4n} rings, the HOMO and LUMO of both out-of-plane and in-plane orientations are non-degenerate MOs with the same

number of n nodal planes and the same symmetry. Hence the symmetry allowed $HOMO_{out/in} \rightarrow LUMO_{out/in}$ excitations, rotating the HOMOs by an angle of $2\pi/4n$, to lead to an optimum overlap producing maximum paratropic response. For example, in C_{16} the rotational excitations of $HOMO_{out}$ and $HOMO_{in}$ with 4 nodal planes rotated by 22.5° lead to a perfect overlap with $LUMO_{out}$ and $LUMO_{in}$ contributing with +63.3 and +64.4 ppm, respectively, to $NICS_{zz}$ (Fig. 8b) and induce very strong long range deshielding cones (Fig. 8a) that

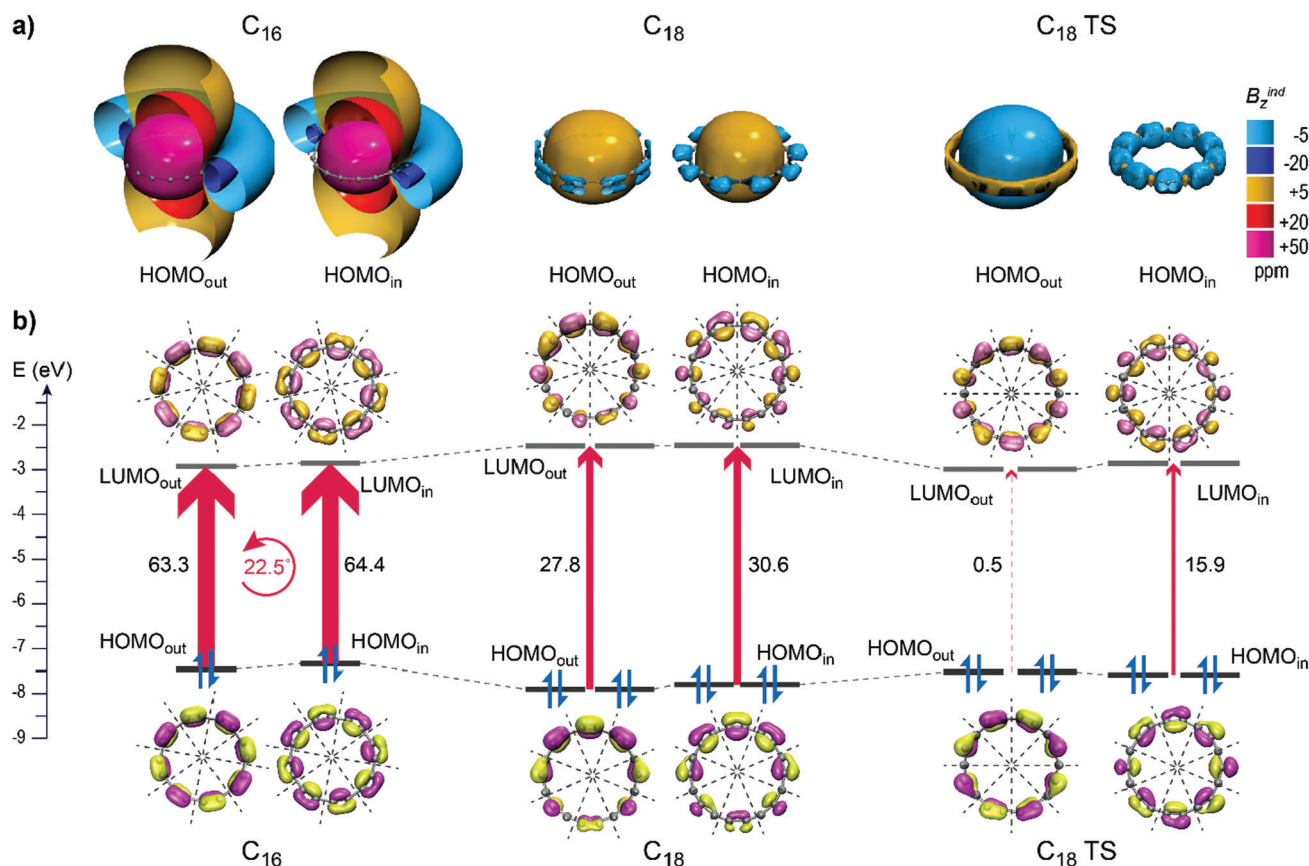**Fig. 8** (a) Isosurfaces of $HOMO_{out}$ and $HOMO_{in}$ contributions to B_z^{ind} of C_{16}, ground state C_{9h} C_{18} and transition state D_{9h} C_{18}. (b) Energy levels and contributions of $HOMO_{out/in} \rightarrow LUMO_{out/in}$ rotational excitations of C_{16}, ground state C_{9h} C_{18} and transition state D_{9h} C_{18}.

dominate on the overall magnetic response. As the HOMO–LUMO gaps remain practically unchanged throughout the C_{4n} series (Table S4, ESI†), the decline in paratropicity originates from a weakening paratropic response of HOMOs and is attributed to the decrease in rotational overlap as the number of nodal planes increases.

In C_{4n+2} rings, both $HOMO_{out}$ and $HOMO_{in}$ are doubly degenerate with n nodal planes, whereas the LUMOs are doubly degenerate with $n + 1$ nodal planes. In a perfect symmetry of D_{nh} point group a HOMO → LUMO rotational excitation would be symmetry forbidden, but in $D_{(n/2)h}$ and $C_{(n/2)h}$ point groups such excitations are symmetry allowed. However due to a different number of nodal planes the overlap is small, inducing a weak magnetic response that depends on the geometrical characteristics of the ring. For example in C_{9h} C_{18}, the frontier orbitals are distorted due to significant BLA and the HOMO → LUMO excitations display a small overlap inducing weak paratropic response (Fig. 8a) that diminishes the diatropicity of the lower energy orbitals, contributing with +27.8 and +30.6 ppm to $NICS_{zz}$ of π_{out} and π_{in}, respectively (Fig. 8b). In contrast, in D_{9h} C_{18} the zero BLA leads to a negligible rotational overlap of $HOMO_{out}$ → $LUMO_{out}$ excitation, resulting in the diatropic response of $HOMO_{out}$ that adds to the overall diatropicity. On the other hand, $HOMO_{in}$ → $LUMO_{in}$ excitations of D_{9h} C_{18} induce small paratropic contributions (+15.9 ppm) due to increased BAA that leads to a weaker diatropicity of π_{in} with regard to π_{out}. The same holds for the ground states of smaller members C_6, C_{10} and C_{14} with zero (or almost zero) BLA, which induce shielding cones from $HOMO_{out}$ (Fig. S5, ESI†) and display increased π_{out} diatropicity. For C_{4n+2} ground states the increment in HOMO nodal planes with the ring size results in a gradual increment in the small overlap and hence in the augmentation of HOMO paratropic contributions (Fig. S5, ESI†), causing a gradual decrement in the overall diatropicity.

Conclusions

The dissection of the induced magnetic field to contributions from out-of-plane and in-plane π orbitals revealed the dual aromatic and antiaromatic character of C_{4n+2} and C_{4n} rings, respectively, according to the magnetic criterion. The magnetic response induced from distinctive sets of electrons is sensitive to the bonding pattern and geometrical features, where polyynic C_{4n+2} ground states display similar out-of-plane and in-plane magnetic responses and comparable diatropicity to annulenes, while the cumulenic transition states exhibit a very strong diatropic character and an augmented out-of-plane magnetic response with regard to the in-plane magnetic response. Bond length alteration is the prime factor that constrains both π_{out} and π_{in} magnetic responses, whereas the bond angle alteration affects secondarily only the π_{in} magnetic response. A significant decline in magnetic response with an increment in the ring size is observed for both ground state aromatic and antiaromatic rings, which is attributed to

decreasing paratropic contributions of HOMOs originating from rotational excitations.

Conflicts of interest

There are no conflicts to declare.

References

1 H. W. Kroto, J. R. Heath, S. C. O'Brien, R. F. Curl and R. E. Smalley, C60: Buckminsterfullerene, *Nature*, 1985, **318**, 162–163.

2 K. S. Novoselov, Electric Field Effect in Atomically Thin Carbon Films, *Science*, 2004, **306**, 666–669.

3 S. Iijima, Helical microtubules of graphitic carbon, *Nature*, 1991, **354**, 56–58.

4 Y. Wang, P. Yang, L. Zheng, X. Shi and H. Zheng, Carbon nanomaterials with sp^2 or/and sp hybridization in energy conversion and storage applications: A review, *Energy Storage Mater.*, 2020, **26**, 349–370.

5 M. F. L. De Volder, S. H. Tawfick, R. H. Baughman and A. J. Hart, Carbon nanotubes: Present and future commercial applications, *Science*, 2013, **339**, 535–539.

6 L. Bacakova, J. Pajorova, M. Tomkova, R. Matejka, A. Broz, J. Stepanovska, S. Prazak, A. Skogberg, S. Siljander and P. Kallio, Applications of Nanocellulose/Nanocarbon Composites: Focus on Biotechnology and Medicine, *Nanomaterials*, 2020, **10**, 196.

7 J. L. Blackburn, A. J. Ferguson, C. Cho and J. C. Grunlan, *Adv. Mater.*, 2018, **30**, 1704386.

8 B. Han, Y. L. Zhang, Q. D. Chen and H. B. Sun, *Adv. Funct. Mater.*, 2018, **28**, 1802235.

9 N. Panwar, A. M. Soehartono, K. K. Chan, S. Zeng, G. Xu, J. Qu, P. Coquet, K. T. Yong and X. Chen, *Chem. Rev.*, 2019, **119**, 9559–9656.

10 A. Rajkamal and R. Thapa, *Adv. Mater. Technol.*, 2019, **4**, 1900307.

11 Y. Jiao, A. Du, M. Hankel and S. C. Smith, Modelling carbon membranes for gas and isotope separation, *Phys. Chem. Chem. Phys.*, 2013, **15**(14), 4832–4843.

12 P. Avouris, M. Radosavljević and S. Wind, Carbon Nanotube Electronics and Optoelectronics, in *Applied Physics of Carbon Nanotubes*, ed. S. V. Rotkin and S. Subramoney, NanoScience and Technology, Springer, Berlin, Heidelberg, 2005.

13 R. H. Baughman, H. Eckhardt and M. Kertesz, Structure-property predictions for new planar forms of carbon: Layered phases containing sp^2 and sp atoms, *J. Chem. Phys.*, 1987, **87**, 6687–6699.

14 F. Diederich, Y. Rubin, C. B. Knobler, R. L. Whetten, K. E. Schriver, K. N. Houk and Y. Li, All-Carbon Molecules: Evidence for the Generation of Cyclo[18]carbon from a Stable Organic Precursor, *Science*, 1989, **245**, 1088–1090.

15 X. Gao, H. Liu, D. Wang and J. Zhang, Graphdiyne: synthesis, properties, and applications, *Chem. Soc. Rev.*, 2019, **48**, 908–936.

This journal is © the Owner Societies 2020

Phys. Chem. Chem. Phys., 2020, **22**, 9240–9249 | **9247**

16 C. Xie, N. Wang, X. Li, G. Xu and C. Huang, Research on the Preparation of Graphdiyne and Its Derivatives, *Chem. – Eur. J*, 2020, **26**, 569–583.

17 R. Sakamoto, N. Fukui, H. Maeda, R. Matsuoka, R. Toyoda and H. Nishihara, The Accelerating World of Graphdiynes, *Adv. Mater.*, 2019, **31**, 1804211.

18 K. Kaiser, L. M. Scriven, F. Schulz, P. Gawel, L. Gross and H. L. Anderson, An sp-hybridized molecular carbon allotrope, cyclo[18]carbon, *Science*, 2019, **365**, 1299–1301.

19 P. W. Fowler, N. Mizoguchi, D. E. Bean and R. W. A. Havenith, Double Aromaticity and Ring Currents in All-Carbon Rings, *Chem. – Eur. J.*, 2009, **15**, 6964–6972.

20 K. Remya and C. H. Suresh, Carbon rings: a DFT study on geometry, aromaticity, intermolecular carbon–carbon interactions and stability, *RSC Adv.*, 2016, **6**, 44261–44271.

21 C. Neiss, E. Trushin and A. Görling, The Nature of One-Dimensional Carbon: Polyynic versus Cumulenic, *ChemPhysChem*, 2014, **15**, 2497–2502.

22 M. Feyereisen, M. Gutowski, J. Simons and J. Almlöf, Relative stabilities of fullerene, cumulene, and polyacetylene structures for Cn: $N = 18$–60, *J. Chem. Phys.*, 1992, **96**, 2926–2932.

23 V. Parasuk, J. Almlof and M. W. Feyereisen, The [18] all-carbon molecule: cumulene or polyacetylene?, *J. Am. Chem. Soc.*, 1991, **113**, 1049–1050.

24 D. A. Plattner and K. N. Houk, C18 Is a Polyyne, *J. Am. Chem. Soc.*, 1995, **117**, 4405–4406.

25 T. Torelli and L. Mitas, Electron Correlation in C4N + 2 Carbon Rings: Aromatic versus Dimerized Structures, *Phys. Rev. Lett.*, 2000, **85**, 1702–1705.

26 S. Arulmozhiraja and T. Ohno, CCSD calculations on C14, C18, and C22 carbon clusters, *J. Chem. Phys.*, 2008, **128**, 114301.

27 A. J. Stasyuk, O. A. Stasyuk, M. Solà and A. A. Voityuk, Cyclo[18]carbon: the smallest all-carbon electron acceptor, *Chem. Commun.*, 2020, **56**, 352–355.

28 G. V. Baryshnikov, R. R. Valiev, A. V. Kuklin, D. Sundholm and H. Ågren, Cyclo[18]carbon: Insight into Electronic Structure, Aromaticity, and Surface Coupling, *J. Phys. Chem. Lett.*, 2019, **10**, 6701–6705.

29 É. Brémond, Á. J. Pérez-Jiménez, C. Adamo and J. C. Sancho-García, Sp-hybridized carbon allotrope molecular structures: An ongoing challenge for density-functional approximations, *J. Chem. Phys.*, 2019, **151**, 211104.

30 A. Nandi, E. Solel and S. Kozuch, Carbon Tunneling in the Automerization of Cyclo[18]carbon, *Chem. – Eur. J.*, 2020, **26**, 625–628.

31 R. Hoffmann, Chemical Abstracts Service: Cumulenes, polyenes, polyacetylenes and cn, *Tetrahedron*, 1966, **22**, 521–538.

32 M. D. Wodrich, C. Corminboeuf, S. S. Park and P. Von Ragué Schleyer, Double aromaticity in monocyclic carbon, boron, and borocarbon rings based on magnetic criteria, *Chem. – Eur. J.*, 2007, **13**, 4582–4593.

33 R. Gershoni-Poranne and A. Stanger, Magnetic criteria of aromaticity, *Chem. Soc. Rev.*, 2015, **44**, 6597–6615.

34 M. K. Cyrański, Energetic Aspects of Cyclic Pi-Electron Delocalization: Evaluation of the Methods of Estimating Aromatic Stabilization Energies, *Chem. Rev.*, 2005, **105**, 3773–3811.

35 J. Poater, M. Duran, M. Solà and B. Silvi, Theoretical Evaluation of Electron Delocalization in Aromatic Molecules by Means of Atoms in Molecules (AIM) and Electron Localization Function (ELF) Topological Approaches, *Chem. Rev.*, 2005, **105**, 3911–3947.

36 D. W. Szczepanik, M. Solà, M. Andrzejak, B. Pawełek, J. Dominikowska, M. Kukułka, K. Dyduch, T. M. Krygowski and H. Szatylowicz, The role of the long-range exchange corrections in the description of electron delocalization in aromatic species, *J. Comput. Chem.*, 2017, **38**, 1640–1654.

37 G. Merino, T. Heine and G. Seifert, The Induced Magnetic Field in Cyclic Molecules, *Chem. – Eur. J.*, 2004, **10**, 4367–4371.

38 R. Islas, T. Heine and G. Merino, The Induced Magnetic Field, *Acc. Chem. Res.*, 2012, **45**, 215–228.

39 R. Gershoni-Poranne and A. Stanger, The NICS- XY -Scan: Identification of Local and Global Ring Currents in Multi-Ring Systems, *Chem. – Eur. J.*, 2014, **20**, 5673–5688.

40 R. Gershoni-Poranne and A. Stanger, Magnetic criteria of aromaticity, *Chem. Soc. Rev.*, 2015, **44**, 6597–6615.

41 I. G. Cuesta, A. S. De Merás, S. Pelloni and P. Lazzeretti, Understanding the ring current effects on magnetic shielding of hydrogen and carbon nuclei in naphthalene and anthracene, *J. Comput. Chem.*, 2009, **30**, 551–564.

42 R. Benassi, P. Lazzeretti and F. Taddei, Magnetic criteria for aromaticity, *J. Phys. Chem.*, 1975, **79**, 848–851.

43 N. D. Charistos, A. G. Papadopoulos and M. P. Sigalas, Interpretation of Electron Delocalization in Benzene, Cyclobutadiene, and Borazine Based on Visualization of Individual Molecular Orbital Contributions to the Induced Magnetic Field, *J. Phys. Chem. A*, 2014, **118**, 1113–1122.

44 N. D. Charistos, A. G. Papadopoulos, T. A. Nikopoulos, A. Muñoz-Castro and M. P. Sigalas, Canonical orbital contributions to the magnetic fields induced by global and local diatropic and paratropic ring currents, *J. Comput. Chem.*, 2017, **38**, 2594–2604.

45 N. D. Charistos and A. Muñoz-Castro, Double aromaticity of the B 40 fullerene: induced magnetic field analysis of π and σ delocalization in the boron cavernous structure, *Phys. Chem. Chem. Phys.*, 2019, **21**, 20232–20238.

46 N. D. Charistos, A. Muñoz-Castro and M. P. Sigalas, The pseudo-π model of the induced magnetic field: fast and accurate visualization of shielding and deshielding cones in planar conjugated hydrocarbons and spherical fullerenes, *Phys. Chem. Chem. Phys.*, 2019, **21**, 6150–6159.

47 J. Da Chai and M. Head-Gordon, Long-range corrected hybrid density functionals with damped atom-atom dispersion corrections, *Phys. Chem. Chem. Phys.*, 2008, **10**, 6615–6620.

48 A. Ehnbom, M. B. Hall and J. A. Gladysz, Origin of Shielding and Deshielding Effects in NMR Spectra of Organic Conjugated Polyynes, *Org. Lett.*, 2019, **21**, 753–757.

49 M. J. Frisch, G. W. Trucks, H. B. Schlegel, G. E. Scuseria, M. A. Robb, J. R. Cheeseman, G. Scalmani, V. Barone, G. A. Petersson, H. Nakatsuji, X. Li, M. Caricato,

9248 | *Phys. Chem. Chem. Phys.*, 2020, **22**, 9240–9249

This journal is © the Owner Societies 2020

A. Marenich, J. Bloino, B. G. Janesko, R. Gomperts, B. Mennucci, H. P. Hratchian, J. V. Ortiz, A. F. Izmaylov, J. L. Sonnenberg, D. Williams-Young, F. Ding, F. Lipparini, F. Egidi, J. Goings, B. Peng, A. Petrone, T. Henderson, D. Ranasinghe, V. G. Zakrzewski, J. Gao, N. Rega, G. Zheng, W. Liang, M. Hada, M. Ehara, K. Toyota, R. Fukuda, J. Hasegawa, M. Ishida, T. Nakajima, Y. Honda, O. Kitao, H. Nakai, T. Vreven, K. Throssell, J. A. Montgomery, Jr., J. E. Peralta, F. Ogliaro, M. Bearpark, J. J. Heyd, E. Brothers, K. N. Kudin, V. N. Staroverov, T. Keith, R. Kobayashi, J. Normand, K. Raghavachari, A. Rendell, J. C. Burant, S. S. Iyengar, J. Tomasi, M. Cossi, J. M. Millam, M. Klene, C. Adamo, R. Cammi, J. W. Ochterski, R. L. Martin, K. Morokuma, O. Farkas, J. B. Foresman and D. J. Fox, *Gaussian 09*, Gaussian, Inc., Wallingford CT, 2016.

50 G. te Velde, F. M. Bickelhaupt, E. J. Baerends, C. Fonseca Guerra, S. J. A. van Gisbergen, J. G. Snijders and T. Ziegler, Chemistry with ADF, *J. Comput. Chem.*, 2001, **22**, 931–967.

51 ADF, *SCM, Theoretical Chemistry*, Vrije Universiteit, Amsterdam, The Netherlands, 2019, http://www.scm.com.

52 A. D. Becke, A new mixing of Hartree-Fock and local density-functional theories, *J. Chem. Phys.*, 1993, **98**, 1372–1377.

53 J. P. Perdew, K. Burke and M. Ernzerhof, Generalized gradient approximation made simple, *Phys. Rev. Lett.*, 1996, **77**, 3865–3868.

54 G. Schreckenbach and T. Ziegler, Calculation of NMR Shielding Tensors Using Gauge-Including Atomic Orbitals and Modern Density Functional Theory, *J. Phys. Chem.*, 1995, **99**, 606–611.

55 N. Charistos, T. Nikopoulos and M. Sigalas, *MIMAF (Molecular Induced MAgnetic Fields) code*, Laboratory of Quantum and Computational Chemistry, Department of Chemistry, Aristotle University of Thessaloniki, Thessaloniki, 2016.

56 W. Humphrey, A. Dalke and K. Schulten, VMD: Visual molecular dynamics, *J. Mol. Graphics*, 1996, **14**, 33–38.

57 F. Pichierri, Boron-nitrogen analogues of cyclo[18]carbon, *Chem. Phys. Lett.*, 2020, **738**, 136860.

58 C. Corminboeuf, R. B. King and P. von R. Schleyer, Implications of Molecular Orbital Symmetries and Energies for the Electron Delocalization of Inorganic Clusters, *ChemPhysChem*, 2007, **8**, 391–398.

59 I. Pérez-Juste, M. Mandado and L. Carballeira, Contributions from orbital–orbital interactions to nucleus-independent chemical shifts and their relation with aromaticity or anti-aromaticity of conjugated molecules, *Chem. Phys. Lett.*, 2010, **491**, 224–229.

60 C. M. Widdifield and R. W. Schurko, Understanding chemical shielding tensors using group theory, MO analysis, and modern density-functional theory, *Concepts Magn. Reson. Part A*, 2009, **34A**, 91–123.

This journal is © the Owner Societies 2020

Phys. Chem. Chem. Phys., 2020, **22**, 9240–9249 | **9249**